Effect of synthesis duration on the morphological and structural modification of the sea urchin-nanostructured γ-MnO2 and study of its electrochemical reactivity in alkaline medium

Lynda Benhaddad, Cyrille Bazin, Laid Makhloufi, Bouzid Messaoudi, Françoise Pillier, Kamal Rahmouni, Hisasi Takenouti

Effect of synthesis duration on the morphological and structural modification of the sea-urchin nanostructured γ-MnO$_2$ and study of its electrochemical reactivity in alkaline medium

L. Benhaddad[a,b,c]*, C. Bazin[b,c], L. Makhloufi[a], B. Messaoudi[a], F. Pillier[b,c], K. Rahmouni[b,c], H. Takenouti[b,c]

[a]*Laboratoire d'électrochimie, corrosion et de valorisation énergétique (LECVE). Département de Génie des Procédés. A. Mira University, Route de Targa Ouzemmour, 06000 Bejaia, Algeria.*
[b]*CNRS, UPR 15, Laboratoire Interfaces et Systèmes Electrochimiques, (LISE, case courrier 133), 4 Place Jussieu, F-75005, Paris, France*
[c]*UPMC Univ. Paris VI, UPR 15, LISE, (case courrier 133), 4 Place Jussieu, F-75005, Paris, France*

Abstract

Single crystalline nanorods and sea-urchin like morphology of the γ-MnO$_2$ nanostructures were successfully synthesized by hydrothermal method at different synthesis durations. The as-synthesized products were characterized by the techniques X-Ray powder Diffraction (XRD), Field Emission Gun-Scanning Electron Microscope (FEG-SEM) coupled with Energy Dispersive X-ray elemental analysis (EDX), Transmission Electron Microscope (TEM), isotherms of N$_2$ adsorption/desorption and BET-BJH models. The effect of synthesis duration on the morphology, porous structure, and crystallographic form of MnO$_2$ powders was studied. The electrochemical reactivity of as prepared powders was investigated in 1 mol L^{-1} KOH by both cyclic voltammetry and impedance spectroscopy by using a micro-cavity electrode. The results show that the best electrochemical reactivity of the MnO$_2$ powder obtained with synthesis duration of 24 h.

Keywords: MnO$_2$; Nanostructures; Hydrothermal synthesis; Micro-cavity electrode; impedance spectroscopy.

* Corresponding author, E-mail: benhaddad.lynda@gmail.com. Tel: +33 6 3625 6554

1. Introduction

A great attention is directed nowadays towards nanostructured manganese dioxides because of their wide structural diversity combined with their unique physical and chemical properties and so for their many technological applications such as catalysis, batteries, supercapacitors and so on [1-3].

Nanostructured manganese dioxide can be synthesized by electrochemical as well as chemical processes [4-8]. It was reported in the literature the synthesis of various nanostructures of manganese dioxide, such as nanotubes [9], nanowires, nanorods [10], nanoflowers [11], by thermal, sol-gel, soft chemical process, and hydrothermal methods. The effects of pH, concentrations, temperature, reactants, counter-cations, and anions on the structure, crystallinity and morphology of the final products were extensively studied. In our previous papers [6-8], MnO_2 powders were synthesized by hydrothermal method at different synthesizing temperature and different oxidizing agents. The products were presented as the sea-urchin like morphology, which was also obtained by reaction between $MnSO_4$ and $(NH_4)_2S_2O_8$ at 100 °C for 20 h [12], $MnCl_2.4H_2O/(NH_4)_2S_2O_8$ at 90 °C for 12 h and 24 h [13], $KMnO_4$/concentrated HNO_3 at 120 °C for 6 h [14]. We have remarked that the morphology of MnO_2 powder largely depend on the choice of reactants and experimental conditions. Actually, MnO_2 nanowires in a powder form with a diameter of 10-50 nm were synthesized by both hydrothermal method [15] and soft chemical process [16].

As cited above [7], we have synthesized MnO_2 powders at different temperatures (60, 90 and 120 °C) in order to study the influence of this parameter on the morphology, structure, and porosity of the obtained γ-MnO_2 which presents the highest electrochemical reactivity compared to other crystalline varieties. The results showed that this parameter did not influence the morphology of powders, but influences their structures, porosities and their electrochemical reactivities. Indeed, the temperature of 90 °C give rise to the synthesis of γ-

2

MnO$_2$ which is more electrochemically reactive than those synthesized at 60 (ε-MnO$_2$) and 120 °C (β-MnO$_2$). Pang et al. [17] reported the hydrothermal synthesis of well-defined and fully developed α-MnO$_2$ nanorods at 80 °C for 24 h. However, the increase of the temperature at 160 °C results in the formation of α-MnO$_2$ nanowires, in the first stage of reaction, which will be transformed to aggregates of microrods (β-MnO$_2$) with the increase of the synthesis time [18]. These results show that the temperature and synthesis duration play crucial role in accelerating the evolution of the nanostructures of MnO$_2$. Other experimental conditions were also being studied in order to synthesize nanostructured MnO$_2$ powder which presents the highest electrochemical reactivity [19, 20].

Manganese dioxides have many polymorphic forms, such as α-, β-, γ-, δ- and λ- which differ in the way in which the basic octahedral MnO$_6$ units are linked together [21]. The nanostructured γ-MnO$_2$ in powder form is an electrochemically active form, which is commonly used as a cathodic material in Leclanché and alkaline batteries.

The γ-MnO$_2$ form is considered as a ramsdellite matrix with randomly distributed intergrown microdomains of pyrolusite, which are constructed with the basic building block of MnO$_6$ units by edge and corner sharing, forming (1×1) and (1×2) tunnels, respectively [22]. Consequently, the γ-MnO$_2$ displays the most complex structure because it contains defects (De Wolff disorder and microtwinning) [21]. As the physical and chemical properties of MnO$_2$ powders depend strongly on the experimental conditions, great efforts were focused to optimize experimental conditions in order to synthesize a reactive γ-MnO$_2$.

This paper focuses, firstly on the study of the effect of synthesis duration on the morphology, structure, crystallographic form, and the porosity of the MnO$_2$ powders synthesized by hydrothermal method. The structure and morphology of the synthesized powders were characterized by the techniques of FEG-SEM, EDX, TEM and XRD. The methods of Brunauer-Emmett-Teller (BET) and Barret-Joyner-Halenda (BJH) were used to evaluate the

specific surface area and the pore size distribution of the powders, respectively. Secondly, to compare the electrochemical reactivity of the MnO_2 powders in 1 mol L^{-1} KOH by means of cyclic voltammetry and electrochemical impedance spectroscopy with the helps of micro-cavity electrode.

2. Experimental

2.1. Synthesis of MnO_2 powders

All the solutions were prepared using deionised water with double ion exchange columns. Manganese sulphate ($MnSO_4.H_2O$) and ammonium persulphate ($(NH_4)_2S_2O_8$) respectively, reactant and oxidizing agent, were purchased from Prolabo products and used as received.

The manganese dioxide (MnO_2) powders were synthesized by hydrothermal method as reported in our previous papers [6-8]. This method consisted of mixing 0.08 mol of $MnSO_4.H_2O$ and 0.08 mol of $(NH_4)_2S_2O_8$, in 150 mL of deionised water at room temperature. The mixture was stirred during 10 min to form a homogeneous pink solution. This solution was then heated at 90 °C for different synthesizing durations (6 h, 18 h, 24 h and 8 days). The products as precipitate thus obtained were filtered off, rinsed several times with deionised water, and finally dried at 60 °C for 24 h.

The formation of MnO_2 in a powder form occurs according to the following reaction:

$$MnSO_4 + (NH_4)_2S_2O_8 + 2H_2O \rightarrow MnO_2 + (NH_4)_2SO_4 + 2H_2SO_4 \tag{1}$$

The electrochemical reactivity of MnO_2 powders was investigated in 1 mol L^{-1} KOH prepared with KOH (Merck product) and deionised water.

2.2. Characterization of MnO_2 powders

The morphology and the elemental composition of the MnO_2 powders were characterized by Field Emission Gun-Scanning Electron Microscope (FEG-SEM, Ultra 55 Zeiss) coupled with

4

Energy Dispersive X-ray elemental analysis (EDX). In addition to these techniques, the X-ray powder diffraction (XRD) and the transmission electron microscopy (TEM) were also used.

TEM images were obtained with a JEOL 2000 FX microscope running at an accelerating voltage of 200 keV. Prior to analysis, the MnO_2 powder was crushed in a mortar. A small amount was then added in pure ethanol and homogenized with ultrasonic bath. A drop of this mixture was placed on a copper grid covered with a carbon coating, and dried in air before analysis.

The results of the N_2 adsorption/desorption isotherms, the pore size distribution, and BET surface area were determined by the Micromeritics Instrument. Prior to analysis, the powders were purged under vacuum at 80 °C to remove surface water, which would interfere with the instrument. The N_2 adsorption/desorption isotherms were then collected at 77 K. The pore size distribution and the surface areas of the samples were measured using the models Barrett-Joyner-Halenda (BJH) and Brunauer-Emmett-Teller (BET) models, respectively.

2.3. Experimental devices

The electrochemical experiments were usually carried out in a three electrode cell: micro-cavity electrode as working electrode, calomel reference electrode in saturated KCl solution (SCE), and a platinum grid of large surface area as counter electrode. The micro-cavity electrode was made of platinum wire (60 μm in diameter) sealed in a glass tube (8 mm in diameter) [23, 24]. A small cylindrical cavity (50 μm in diameter and 25 μm in depth) was formed by a laser ablation of the platinum wire. This cavity was filled with the MnO_2 powder using the electrode as a pestle. This method constituted a marked advantage to study the MnO_2 powder itself. First, the electrode was formed without any additive to give cohesion of powder. Second, the electrochemical process taking place at the substrate/electrolyte interface was negligible. Third, a thin powder layer allowed the minimization of the in-depth

distribution of both potential and current, and finally, only a small amount of MnO_2 is needed. The volume of the cavity used was $50 \cdot 10^{-9}$ cm^3 [23, 24]. With the apparent specific gravity of MnO_2 powder estimated at 2.2, the mass necessary will be 110 ng to perform experiments. The grinding of MnO_2 into a fine powder before its introduction into the cavity permitted likely to homogenise MnO_2 powder to be analysed. Consequently, this method also allowed the achievement of well-reproducible results.

Electrochemical measurements, including cyclic voltammetry (CV) and electrochemical impedance spectroscopy (EIS) were carried out with a Potentiostat allowing determining low current and huge impedance (Gamry, Femstat FAS1). Both, the potentiostat and the electrochemical cell were set in a Faraday cage. The electrochemical impedance spectroscopy (EIS) measurements were carried out on the open circuit potential just before the beginning of each experiment with ac amplitude of 10 mV in the frequency range from 10 kHz to 1 mHz by 10 points per decade. The impedance data were analyzed with in-house made software based on a simplex parameter regression.

3. Results and discussion

3.1. Characterization of MnO_2 powders

The X-ray diffraction patterns of the powders obtained at different synthesis durations are presented at Figure 1. It can be seen that all patterns have similar peaks which are assigned to the values of (hkl) 120, 031, 131, 230, 300, 160, 401, 421, 062, and 450. All these peaks can be indexed to the crystallographic form γ-MnO_2, which is in agreement with the reference (JCPDS Card no. 14-0644). However, others peaks are also detected and assigned to the values of (hkl) 200, 310, 411, 521, 541 and 332 as marked inside box.

These peaks can be indexed to the crystallographic form α-MnO_2 according to the reference (JCPDS Card no. 44-0141). It can be noted from Figure 1 (a) that the increase of synthesis

duration of 6 h to 18 h leads to the increase of all peaks intensities. However, the pattern corresponding to MnO_2 synthesized at 24 h shows also an increase in the intensity of the peaks of γ-MnO_2, indicating a more crystalline product. However, the intensity of the peaks of α-MnO_2 decreases indicating the disappearance of this form from the structure of γ-MnO_2, which allows us to consider this product as a pure γ-MnO_2.

Figure 1 (b) shows that the increase of synthesis duration of 24 h to 8 days does not affects the intensity of the peaks of γ-MnO_2 as shown by the superposition of the two patterns, but it can be well observed the increase of the intensity of the peaks of α-MnO_2, which reveals the reappearance of this crystallographic form and consequently the synthesized γ-MnO_2 powder for 8 days is not pure. Then, no further characterizations were applied to this powder.

<Figure 1>

Fu et al. [25] reported that the synthesis of the pure crystalline γ-MnO_2 depends strongly on the synthetic conditions such as the molar ratio (reactant/oxidant) which must be larger than 2.3 ($MnSO_4/KMnO_4 \geq 2.3$). Also, these authors [25] reported that the excess amount of Mn^{2+} in solution enhances two important phenomena: (a) crystallization of γ-MnO_2 in short nanorods from poorly ordered nanoparticles; (b) formation of γ-MnO_2 in hollow structures. Wang and Li [26] prepared β-MnO_2 from a reaction between $MnSO_4$ and $(NH_4)_2S_2O_8$; however, after the addition of $(NH_4)_2SO_4$ the β-MnO_2 transform into α-MnO_2. It was reported that the cations (eg. K^+ and NH_4^+) are believed to be able to serve as inorganic templates for the formation of α-MnO_2 [27]. In our previous paper [7], we have remarked that the formation of γ-MnO_2 occurred at 90 °C and it is stable in the course of time. The γ-MnO_2 synthesized from a reaction between $MnSO_4$ and $(NH_4)_2S_2O_8$ at 160 °C was rapidly transformed to β-MnO_2 which is the most stable form at high temperatures compared to other varieties [12, 18].

The FEG-SEM images of the MnO_2 powders are presented at Figure 2. The morphology of the powders synthesized at 6 h, 18 h and 24 h is similar and is presented as the sea-urchin microparticles composed of many nanowires heaped together. It can be well observed that the diameter and the length of the nanowires increase with the increase of synthesis duration. It is well observed that the synthesis duration of 24 h leads to the formatin of sea-urchin microparticles covered with numerous crystalline and well-ordered nanowires. Also, it was reported in the literature, the hydrothermal synthesis of the sea-urchin particles of α-MnO_2 [28], and of β-MnO_2 [29] covered by nanowires and nanorods, respectively. In our previous paper [6], the sea-urchin particles of γ-MnO_2 covered by nanoneedles were synthesized from a reaction between $MnSO_4$ and $Na_2S_2O_8$ at 90 °C for 24 h.

However, the use of the oxidizing agent $(NH_4)_2S_2O_8$ leads to the synthesis of sea-urchin particles covered with nanowires as obtained in the present paper. Also, the increase of synthesis duration engenders an increase of the nanowires size and transformation of the sea-urchin particles to nanorods which shows that this parameter influences the morphology and the crystallographic form of the MnO_2 powders. In our previous paper [7] we remarked that the synthesis temperature equal or less than 120 °C affects the crystallographic form of MnO_2 powders but did not influences their morphologies. Zhou et al. [1] and Gao et al. [12] reported that the increase of temperature more than 120 °C induces significant changes in the morphology and the crystallographic form of MnO_2.

<Figure 2>

Elemental analysis by EDX (Figure 3) confirms the presence of manganese and oxygen which compose the MnO_2. On the all profiles, the presence of manganese is shown by two energy peaks appearing approximately at 6 and 6.5 keV whereas that of oxygen is shown by one

energy peak situated approximately at 0.5 keV. The presence of the sulphur coming from manganese sulphate is negligible.

<Figure 3>

The typical TEM images shown at Figure 4 indicate that the tiny wires of MnO_2 powders, observed by SEM technique, depends on the synthesis duration. It can be observed that few nanowires are presented in the powders synthesized for 6 h and 18 h and that the number and the crystallinity of these nanowires increase with the increase of synthesis duration. The MnO_2 synthesized for 24 h consisted of assembling of crystalline, straight wires with diameters in the range of 30-50 nm and lengths up to several hundred nanometers.

<Figure 4>

The N_2 adsorption/desorption isotherms of MnO_2 powders obtained with different synthesis duration are presented at Figure 5. These isotherms are of typical IV classification exhibiting the H3-type hysteresis loop which are characteristic of mesoporous materials. The three isotherms are characterized by a gradual increase of adsorbed gas, as a function of relative pressure, due to the condensation of the adsorbate in larger pores formed between particles. This phenomenon was observed with different particle size distributions of the same material [30, 31]. As the desorption process is not reversible, these isotherms exhibit a substantial hysteresis loop in the P/P_0 range above 0.6 characteristics of mesoporous materials.

<Figure 5>

The pore size distribution of the three MnO_2 powders determined by BJH method and the pore properties are presented at Figure 6 and table 1, respectively. The Figure 6 shows that MnO_2 powders consist of the mesoporous distribution. The MnO_2 powder synthesized for 6 h presents a pore size distribution between 2 and 50 nm with the quasi-total absence of

micropores and macropores. The increase of synthesizing duration to attain 18 h leads to the enlargement of pores between 5 and 100 nm accompanied with the increase of pore volume.

However, two kinds of porosity can be observed from the pore size distribution corresponding to the MnO_2 powder synthesized for 24 h: macropores with a maximum located between 70 and 100 nm and mesopores with a maximum between 20 and 30 nm. As presented in table 1, the total pore volume of the powders increases with the increase of synthesis duration leading to a more porous powder.

<Figure 6>

The surface area of each powder was determined by the BET isotherm in conjunction with N_2 adsorption data collected over the relative pressure range between 0.06 and 0.2 at 77 K. In fact, at low relative pressures the isotherm underpredicts actual adsorption since the adsorption energies is higher than the expected value because of the surface inhomogeneity. In contrast, at high relative pressures, the BET isotherm overestimates adsorption because of limitations associated with liquefaction on the adsorbate [30]. The BET isotherm is expressed as follows:

$$\frac{P}{V_a(P_0 - P)} = \frac{1}{V_m C} + \frac{C-1}{V_m C}\frac{P}{P_0} \tag{2}$$

Where, V_a is the volume of gas adsorbed at P/P_0 (cm^3 g^{-1}); V_m is the volume of gas that would occupy a monolayer (cm^3 g^{-1}); C is a constant for the gas/solid pair; P and P_0 are the equilibrium and the saturation pressures of adsorbate at the temperature of adsorption, respectively. The values of V_m and C can be evaluated from the plot $P/(V_a(P_0-P))$ versus P/P_0 and consequently, the expanded surface area is calculated from the following expression:

$$S = 4.35\ V_m \tag{3}$$

It is noteworthy that the total surface area of a porous electrode is the sum of the surface area of all pores [31]. As recorded in table 1, the surface area increases with increasing synthesis duration due to the enlargement of pores and to the apparition of macropores. The surface area of MnO_2 is generally comprised between 50 and 70 m^2 g^{-1}, which is the case of MnO_2 powders synthesized for 6 h and 18 h. However, the surface area of MnO_2 synthesized for 24h is therefore significantly larger than the value usually reported in the literature.

3.2. Electrochemical reactivity of MnO₂ powders

The cyclic voltammetry and impedance spectroscopy techniques using a micro-cavity electrode were applied to characterize the electrochemical reactivity in 1 mol L^{-1} KOH of MnO_2 powders synthesized at different durations.

3.2.1. Cyclic Voltammetry

The micro-cavity electrode containing the MnO_2 powder was transferred into 1 mol L^{-1} KOH at ambient temperature without purging dissolved oxygen. Then, after one minute of stabilization time at the open circuit potential, the cyclic voltammetry measurements were carried out. The potential scan rate was 0.2 V s^{-1} and started from the open-circuit potential towards the negative direction up to -0.7 V (vs. SCE), followed by the anodic scan up to 0.6 V (vs. SCE). Figure 7 presents cyclic voltammograms obtained at the first cycle. The results show that both anodic and cathodic peaks detected in the three cases are located at the same potential domain, thus they are ascribed to the same reactions. The comparison of these voltammograms shows the increase of cathodic and anodic peak intensities with the increase of synthesis duration of 6 h to 24 h. Therefore, the MnO_2 powder synthesized in 24 h has the highest electrochemical reactivity in 1 mol L^{-1} KOH.

<Figure 7>

11

From these voltammograms and during the cathodic scan, a current peak is observed clearly at around -0.4 V (vs. SCE) which is attributed to the reduction of MnO_2 to $MnOOH$ by the diffusion of protons in the lattice of MnO_2 according to the reaction (4).

$$MnO_2 + H^+ + e^- \rightarrow MnOOH \qquad (4)$$

Kozawa and Yeager [32] have proposed a mechanism with two steps for the reduction of MnO_2 from an alkaline medium. In the first step, an electron is inserted from the external circuit of the structure of MnO_2 for the reduction of Mn^{4+} in Mn^{3+}. To maintain the electroneutrality of the reaction, a water molecule, which is present at the interface MnO_2/electrolyte dissociates to give one proton H^+, which will inserted in the structure of MnO_2 while the ions OH^- remains in solution. M. Minakshi [33] has studied the behaviour of MnO_2 in an alkaline medium of KOH by using microscopic techniques. The results suggest that the electrode reaction of MnO_2 in this electrolyte is the insertion of potassium (K^+), in addition to the usual protonation i.e. insertion of H^+ during the discharge process.

In aqueous solution, Toupin et al. [34] have proposed two possible mechanisms to explain this phenomenon. The first implicates the insertion of the protons (H^+, Eq. 4) or the metallic cations (K^+, Eq. 5) into the matrix of MnO_2 during the reduction followed by their expulsion during the oxidation reaction.

$$MnO_2 + K^+ + e^- \rightarrow MnOOK \qquad (5)$$

The second mechanism presented by reaction (6) is expected to be predominant in the crystalline MnO_2 and involves the insertion/expulsion of protons (H^+) or cations (M^+) into the material bulk:

$$(MnO_2)_{surface} + K^+ + e^- \rightarrow (MnO_2^-K^+)_{surface} \qquad (6)$$

The diffusion of protons and the facility with which they are inserted into the MnO_2 matrix is widely admitted as the key electrochemical property during the discharge of this material and

it is related in major part to the porosity of MnO_2 [34-36] and/or to its hydration [37]. The presence of protons was identified by neutronic spectroscopy by Cachet et al. [38].

According to Tedjar and Guitton [37], the reduction of the varieties γ-, ε-, δ-MnO_2 is realized by the insertion of protons by jumping from a water molecule to another and that the more hydrated form has a higher electrochemical reactivity.

It was reported in the literature that the cathodic peak can be attributed to both reduction of MnO_2 and reduction of dissolved oxygen since they have a potential very close in alkaline medium [39,40]. The mechanism of the oxygen reduction was proposed to be a coupled reaction involving the redox pair $MnO_2/MnOOH$ [41].

During the anodic scan, a current peak was observed on the three voltammograms at a potential around 0.3 V (vs. SCE). This peak corresponds to the oxidation of MnOOH formed previously to MnO_2 according to the reverse reaction of (4 or 5). The intensity of this peak is better in the case of MnO_2 synthesized for 24h.

The cathodic charge used for the reduction of MnO_2 (j < 0) as function of the scan's number for the MnO_2 powders synthesized at different durations is presented at Figure 8. It can be well observed that the cathodic charge increases with the increase of the synthesis duration and the scan's number increase which means that the powder synthesized for 24 h is the most reactive form in the test medium compared to other powders.

<Figure 8>

13

The cathodic charge of the MnO$_2$ powder synthesized in 24 h as function of scan's number of different scan rates is presented at Figure 9. As observed, the increase of the scan rate engenders a decrease of the cathodic charge which corresponds to the decrease of the amount of charges inserted in the structure of MnO$_2$. From this, it can be concluded that the insertion of protons into the structure of MnO$_2$ is slow which requires a longer time. It was also observed that the cathodic charge increases with the increase of scan's number at a scan rate of 0.2 V.s^{-1} while it is stable in the other cases.

<Figure 9>

The micro-cavity electrode containing the MnO$_2$ powder was transferred into 1 mol L^{-1} KOH and after different stabilization time at the open circuit potential (30 s, 60 s, 10 min and 30 min), the cyclic voltammetry measurements were carried out. The potential scan rate was 0.2 V s^{-1} and the scan started from the open-circuit potential towards the negative direction up to -0.7 V (vs. SCE), followed by the anodic scan up to 0.6 V (vs. SCE).

The cathodic charge as function of the scan's number for different stabilization times is determined and the results are presented at Figure 10. From this figure, it can be well observed that the increase of stabilization time from 30 sec to 60 sec engenders an increase of the cathodic charge due to the insertion of charges into the structure of MnO$_2$ during the stabilization time. However, the increase of stabilization time to 10 min and 30 min causes the decrease of the cathodic charge which is due probably to the occupation of all active sites of the MnO$_2$ powder by charges or to its deterioration in the test medium. It can be observed that the cathodic charge of the MnO$_2$ powder still constant for stabilization times equal or greater than 10 min which reveals that the amount of charges inserted into the structure of MnO$_2$ is limited.

<Figure 10>

As reported above, the MnO$_2$ powder synthesized for 24 h presents the highest electrochemical reactivity in 1 mol L^{-1} KOH compared with other powders. This is due probably to its porosity, its nanostructured form, or to its crystallographic form γ-MnO$_2$ recognized as the most reactive form. It is difficult to determine the major factor which is responsible for the high reactivity of this powder in the test medium, but, we think that each parameter can contribute. A detailed discussion is presented in section 3.3.

3.2.2. Electrochemical Impedance Spectroscopy

Nyquist impedance spectra presented at Figure 11 were obtained in 1 mol L^{-1} KOH in the frequency range from 10 kHz to 1 mHz after ageing with cyclic voltammetry for 10 scans at 0.2 V s^{-1}. The EIS diagrams exhibit though badly separated two capacitive loops in high and medium frequency range and a linear branch in the lower frequencies corresponding to the diffusion of protons into the lattice of MnO$_2$. The slope of this linear branch is different for the three powders.

<Figure 11>

The recorded data may be represented by an equivalent electrical circuit named 2RC-C shown at Figure 12. In this circuit, R_e represents the electrolyte resistance between the reference and the working electrode; R_t and C_d are allocated, respectively, to the charge transfer resistance in parallel with the double layer capacitance; R_F and C_F stand for faradaic impedance associated with the reduction of dissolved oxygen; C_{ac} characterizes the capacitance corresponding to charge storage in the chemical form, i.e. corresponding to a proton (H$^+$) insertion/expulsion process. This capacitance is therefore the determining parameter in the use of MnO$_2$ as battery material; n_d, n_F, n_{ac} are allowed reproducing a depressed feature of impedance diagram in Nyquist plane (Cole-Cole coefficient), and they will be valued between 0 and 1.

<Figure 12>

To compare the electrochemical reactivity of MnO_2 powders in the test medium, it is appropriate to evaluate the values of the capacitance C_{ac} by using a simplex parameter regression. As reported above, the diagrams are presented as two badly separated capacitive loops and a linear branch. It was considered that the couple R_t/C_d exhibits the highest frequency range (centered at about 315 Hz) and the couple R_F/C_F exhibit the medium frequency range (centered at about 0.1 Hz). The capacitance C_{ac} expresses itself in the lowest frequency range.

The parameter regression shows that the best value of the capacitance C_{ac} is equal to 7.1 μF corresponding to the MnO_2 powder synthesized for 24 h showing its high electrochemical reactivity in the test medium compared with other powders, which confirms cyclic voltammetry results. The regression results show also a decrease of charge transfer and faradaic resistances (R_F), associated with the reduction of dissolved oxygen, with the increase of synthesis duration. As reported above, the mechanism of the oxygen reduction involves the redox reaction between MnO_2 and $MnOOH$ initiated by the diffusion of protons. Therefore, the decrease of faradaic resistance reveals the ease in which protons are inserted into the structure of MnO_2 powder synthesized for 24 h thus leading to the reduction of MnO_2 into $MnOOH$ and consequently in the reduction of dissolved oxygen. Mao et al. [42] showed that $MnOOH$ exhibits the highest catalytic activity for the electrochemical reduction of dissolved oxygen among the various varieties of manganese oxides.

The effect of powder ageing was examined by submitting the γ-MnO_2 powder synthesized at 90 °C for 24 h to cyclic voltammetry in 1 mol L^{-1} KOH for 10 scans at 0.01 V s^{-1} followed by its characterization by EIS measurements in the frequency range from 10 kHz to 10 mHz. The obtained diagram was compared with that recorded before potential cycling. The diagrams presented at Figure 13 exhibit two capacitive loops and a capacitive linear branch at low

frequencies. It was observed that the ageing of MnO_2 powder in the test medium leads to the enlargement of the Nyquist diagram indicating an increase of charge transfer and the faradaic resistances in parallel with a decrease of the capacitance C_{ac}. Indeed, the ageing of MnO_2 powder in the medium leads to the insertion of large amount of charges into its structure. The free active sites will be occupied by charges which engenders the increase of the resistances of faradaic and charge transfer. So, it can be concluded that the ageing of MnO_2 powder in the test medium engenders the decrease of its active sites and/or to its mechanical failure during cycling which provoke to the decrease of its capacitance C_{ac}.

<Figure 13>

3.3. Discussion

The defects have been considered as one of the most crucial factors to determine the electrochemical performance of γ-MnO_2 materials, and have been studied intensively [43-45]. According to Chabre and Pannetier [21], two types of defects are present. The first one is De Wolff disorder, which is formed from the insertion of pyrolusite structural units into ramsdellite matrix, relating to the amount of pyrolusite units. The second type is called microtwinning defects, which are generated by twinning in (021) and (061) planes within the ramsdellite blocks. According to these authors, the Microtwinning defects enhances the electrochemical reactivity of γ-MnO_2 materials whereas De Wolff disorder defects lowers them [21]. However, Balachandran et al. [36] reported that the introduction of microtwinning defects as well as De Wolff disorder can have a large adverse effect on the proton diffusion inside MnO_2. The results showed that the kinetics of γ-MnO_2 reduction is slows down towards the end of discharge attributed to the decrease of proton diffusion which is contradicting with the model of Chabre and Pannetier.

Different mechanisms of the MnO_2 reduction in an alkaline medium were proposed in the literature [43-50]. Burns has suggested that γ-MnO_2 used as cathodic material in batteries might contain lattice defects such as "stacking faults, dislocations, chain defects, etc.". He also suggested that such defects might account for the high water content and the high electrochemical reactivity of γ-MnO_2 [46]. In 1984, P. Ruetschi has proposed a cation-vacancy model for γ- or ε-MnO_2 [45]. In his report, Ruetschi explained that the reason for which γ- and ε-MnO_2 are more reactive than β-MnO_2 is due to the presence of Mn vacancies and corresponding water content thus providing an initial starting concentration of protons for the transfer process. In contrast, β-MnO_2 did not contains almost no vacancies and thus very little structural water. This model was confirmed later by Petit et al [47], Fillaux et al. [48], and Balachandran et al. [49], but contradicted by Tedjar and Guitton [37] and Ananth et al. [50].

As reported previously, Toupin et al. [34] proposed two possible mechanisms to explain the phenomenon of MnO_2 reduction from an aqueous solution. The first implicates the insertion of protons (H^+, Eq. 4) and metallic cations (K^+, Eq. 5) into the matrix of MnO_2. In an alkaline medium, Amarilla et al. [51] reported that the electrochemical behaviour of γ-MnO_2 depends strongly on the KOH concentration. During the discharge process of the first cycle, one step reduction in 1 mol L^{-1} KOH and two step reduction in [KOH] $\geq$ 3 mol L^{-1} were observed. The first reduction step assigned to the insertion process of H^+/e^- increases when the KOH concentration decreases which means that γ-MnO_2 loses its electrochemical reactivity when the concentration of electrolyte increases. Minakshi et al. [33] studied the effect of K^+ ions on the reduction mechanism of MnO_2 from an alkaline medium of KOH 5 mol L^{-1}. The results show the insertion/expulsion of K^+ on the surface of MnO_2, which reduces the electron transfer and therefore a decrease of the electrochemical reactivity. Zhang reported that EMD and CMD display the same XRD patterns, showed a different electrochemical reactivity [52].

Therefore, in such cases, the electrochemical behaviour of these γ-MnO$_2$ powders cannot be properly explained based on the model of Chabre and Pannetier. Zhang considered that this model is extremely useful in dealing with γ-MnO$_2$ materials with a different XRD patterns. For those materials showing little difference in XRD patterns, it is necessary to take into account other factors like differences in physical or chemical properties [52]. Also, Zhang suggested that high porosity and surface area are probably related to the amount of defects presented in the structure of MnO$_2$ which facilitates the protons diffusion and electron transfer during the MnO$_2$ reduction, and therefore outcome high electrochemical reactivity [52]. Indeed, several research projects reported that more the surface area is larger better is the electrochemical behaviour of MnO$_2$ [53-55]. Reddy and Reddy [56] remarked that the specific capacitance of MnO$_2$ depends on the distribution of pore size rather than BET surface area.

However, it was reported in the literature [52] that γ-MnO$_2$ materials of low surface area and high density are more active than light or puffy materials of low density and high surface area probably because in a dense and compact form the electron conduction is facilitated, which was also reported in our previous paper where γ-MnO$_2$ synthesized by Na$_2$S$_2$O$_8$ (40 m^2 g^{-1}) was more reactive in 1 mol L^{-1} KOH than γ-MnO$_2$ synthesized by (NH$_4$)$_2$S$_2$O$_8$ (90.8 m^2 g^{-1}) [6].

Up till now, much works attempts to correlate the physical, chemical and structural properties of γ-MnO$_2$ materials (EMD, CMD, and NMD) with their electrochemical reactivity in batteries but it is still unsolved and remains a key research challenge for researchers in raison of the complexity of γ-MnO$_2$ structure.

4. Conclusions

Two different nanostructures of γ-MnO$_2$ were successfully synthesized by hydrothermal method at different synthesis durations. Indeed, sea urchin particles covered by nanowires

were obtained in the first stage of synthesis which were transformed to nanorods with the increase of synthesis duration. The structural characterization of γ-MnO$_2$ powders shows that the synthesis duration affects the porous structure and the crystallographic form of powders. The study of the electrochemical reactivity of these powders in 1 mol L^{-1} KOH was performed by using micro-cavity electrode. Best results were obtained in the case of γ-MnO$_2$ synthesized for 24 h compared with other synthesized powders.

REFERENCES AND NOTES

1. Zhou L, Zhang J, He J, Hu Y, Tian H (2011) Mater Res Bull 46:1714-1722

2. Cui HJ, Huang HZ, Fu ML, Yuan BL, Pearl W (2011) Catal Comm 12:1339-1343.

3. Jou JH, Shi JW, Liu F, Fu ML (2011) J Mater Chem 21:18527-18529.

4. Cherchour N, Deslouis C, Messaoudi B, Pailleret A (2011) Electrochim Acta 56:9746-9755

5. Messaoudi B, Joiret S, Keddam M, Takenouti H (2001) Electrochim Acta 46:2487-2498

6. Benhaddad L, Makhloufi L, Messaoudi B, Rahmouni K, Takenouti H (2011) J Mater Sci Technol 27:585-593

7. Benhaddad L, Makhloufi L, Messaoudi B, Rahmouni K, Takenouti H (2009) ACS Appl Mater Interfaces 1 (2):424-432

8. Benhaddad L, Makhloufi L, Messaoudi B, Rahmouni K, Takenouti H (2007) Matériaux et Techniques 95:405-410

9. Xiao W, Xia H, Fuh JYH, Lu L (2009) J Power Sources 193:935-938

10. Wang X and Li Y (2003) Chem. Eur J 9 (1):300-306

11. Li Y, Wang J, Zhang Y, Banis MN, Liu J, Geng D, Li R, Sun X (2012) J Colloid Interface Sci 369:123-128

12. Gao T, Fjellvåg H, Norby P (2009) Nanotechnology 20(5):055610-055616

13. Zhou M, Zhang X, Wang L, Wei J, Wang L, Zhu K, Feng B (2011) Mater Chem Phys 130 (3):1191-1194

14. Tang N, Tian X, Yang C, Pi Z (2009) Mater Res Bull 44:2062-2067

15. Liu Y, Zhang M, Zhang J, Qian Y (2006) J Solid State Chem 179:1757-1761

16. Wei M, Konishi Y, Zhou H, Sugihara H, Arakawa H (2005) Nanotechnology 16:245

17. Pang SC, Chin SF, Ling CY (2012) J Nanomaterials Article ID 2012:607870

18. Guan H, Chen G, Zhang S, Wang Y (2010) Mater Chem Phys 124:639-645

19. Wang HE, Qian D, Lu Z, Li Y, Cheng R, Zhang W (2007) J. Cryst. Growth, doi: 10./016/j.jcrysgro.2007.01.034

20. Subramanian V, Zhu H, Vajtai R, Ajayan PM, Wei B (2005) J Phys Chem B 109:20207-20214

21. Chabre Y and Pannetier J (1995) Prog Solid State Chem 23:1-130

22. De Wollf PM (1959) Acta Crystallogr 12:341-345

23. Vivier V, Cachet-Vivier C, Wu BL, Cha CS, Nedelec JY, Yu LT (1999) Electrochem Solid-State Lett 2 (8):385-387

24. Vivier V, Cachet-Vivier C, Cha CS, Nedelec JY, Yu LT (2000) Electrochem Commun 2:180-185

25. Fu X, Feng J, Wang H, Ng KM (2009) Nanotechnology 20:375601

26. Wang X and Li YD (2002) J Am Chem Soc 124:2880-2881

27. Liu J, Makwana V, Cai J, Sui SL, Aindow M (2003) J Phys Chem B 107:9185-9194

28. Zhang Z and Mu J (2007) Solid State Commun 141:427-430

29. Ghodbane O, Pascal JL, Favier F (2009) ACS Appl Mater Interfaces 1(5):1130-1139

30. Arnott JB, Williams RP, Pandolfo AG, Donne SW (2007) J Power Sources 165 (2):581-590

31. Qu D. (2003) Electrochim Acta 48 (12):1675-1684

32. Kozawa H, Heager JF (1965) J Electrochem Soc 112:959-963

33. Minakshi M (2008) J Electroanal Chem 616:99-106.

34. Toupin M, Brousse T, Bélanger D (2004) Chem Mater 16:3184-3190

35. Hong Z, Zhenhai C, Xi X (1989) J Electrochem Soc 136 (10):2771-2774

36. Balachandran D, Morgan D, Ceder G (2002) J Solid State Chem 166:91-103

37. Tedjar F and Guitton J (1985) Surface Technology 26 (2):107-115

38. Cachet C, Belushkin A, Natkaniec I, Lecerf A, Fillaux F, Yu LT (1995) Physica B 213-214:827-829

39. Cao YL, Yang HX, Ai XP, Xiao LF (2003) J Electroanal Chem 557:127-134

40. Roche I and Scott K (2010) J Electroanal Chem 638:280-286

41. Brenet JP (1979) J Power Sources 4:183-190

42. Mao L, Sotomura T, Nakatsu K, Nobuharu K, Zhang D, Ohsaka T (2002) J Electrochem Soc 149 (4):A504-A507

43. Ruetschi P and Giovanoli R (1988) J Electrochem Soc 135 (11):2663-2669

44. Parida KM, Kanungo SB, Sant BR (1981) Electrochim Acta 26:435-443

45. Ruetschi P (1984) J Electrochem Soc 131 (12):2737-2744

46. Burns RG (1984) Battery Material Symposium. In A. Kozawa.and M. Nagayama (Ed), Vol I. Brussels 1983, published by BMRA, Cleveland, OH, pp 197

47. Petit F, Lenglet M, Arsène (1993) J Mater Res Bull 28:1093-1100

48. Fillaux F, Cachet CH, Ouboumour H, Tomkinson J, Lévy-Clément C, Yu LT (1993) J Electrochem Soc 140 (3):585-591

49. Balachandran D, Morgan D, Ceder G, Van de Walle A (2003) J Solid-State Chem 173:462-475

50. Ananth MV, Pethkar S, Dakshinamurthi K (1998) J Power Sources 75 (2):278-282

51. Amarilla JM, Tedjar F, Poinsignon C (1994) Electrochim Acta 39 (15):2321-2331

52. Zhang Q (2001) I. Syntheses of Manganese oxides by using microwave heating and conventional heating, II. Syntheses of nanosize materials. Thesis PHD Connecticut University

53. Lee HY, Kim SW. Lee HY (2001) Electrochem Solid-State Lett 4 (3):A19-A22

54. Devaraj S and Munichandraiah N (2005) Electrochem Solid-State Lett 8(7):A373-A377

55. Devaraj S and Munichandraiah N (2007) J Electrochem Soc 154 (10):A901-A909

56. Reddy RN and Reddy RG (2003) J Power Sources 124:330-337
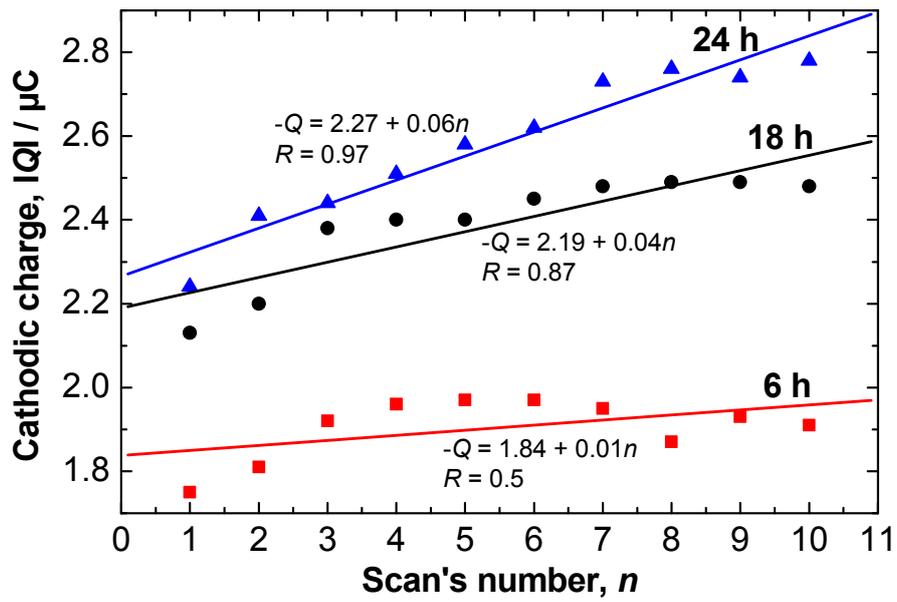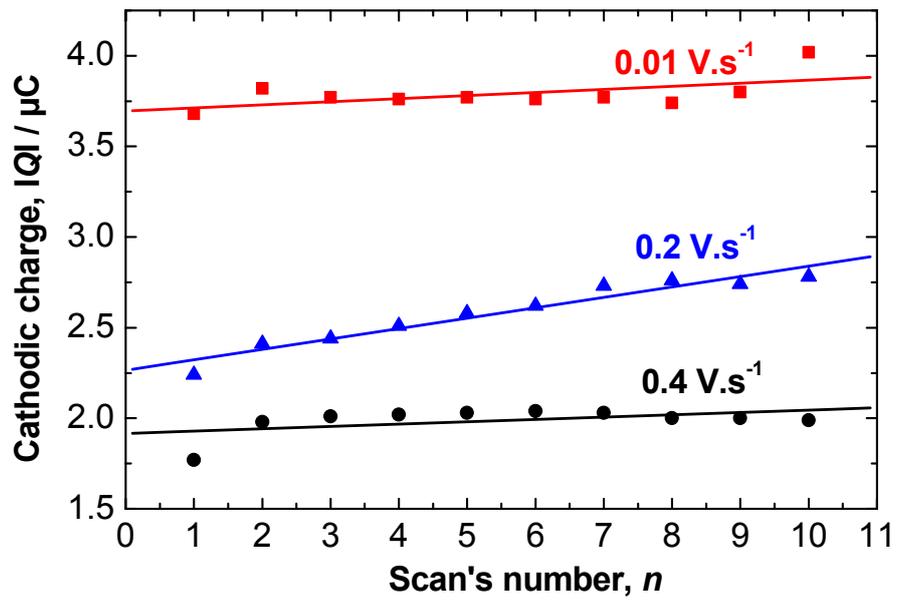
Figure 1
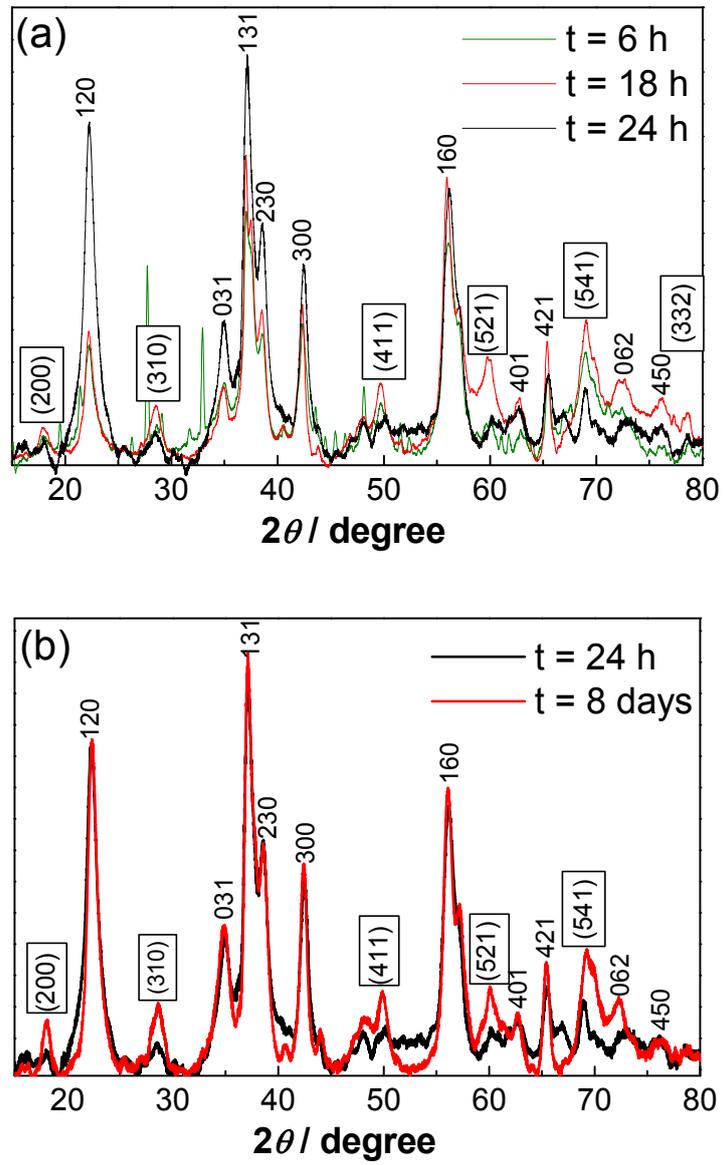
Figure 2.

Figure 3

Figure 4

5
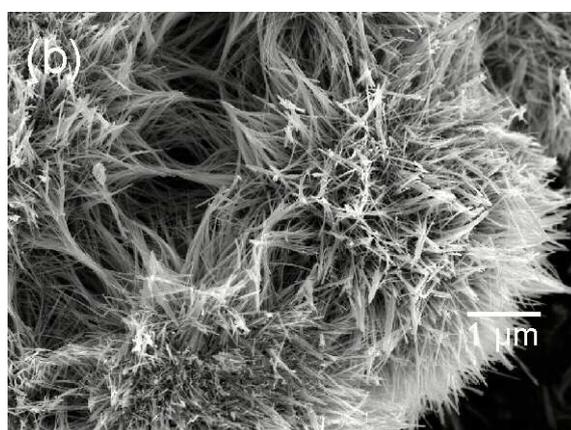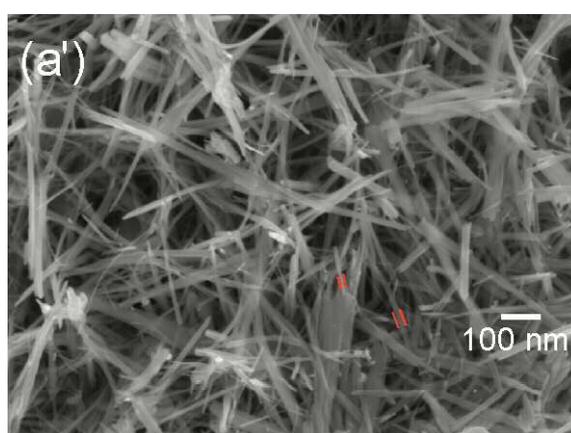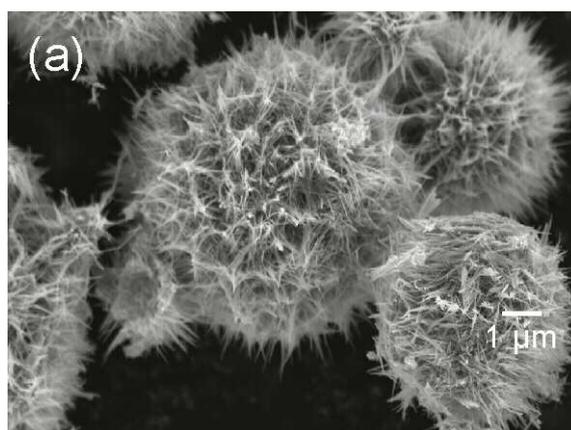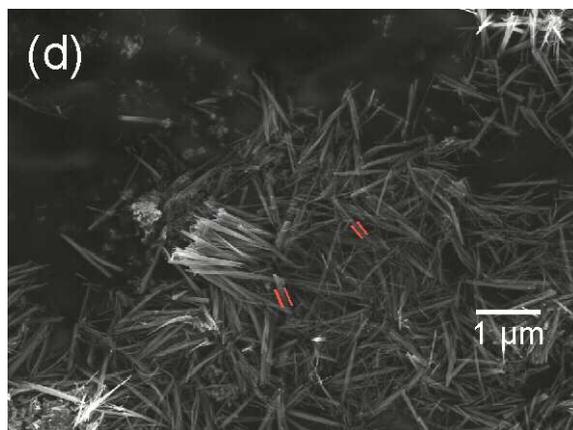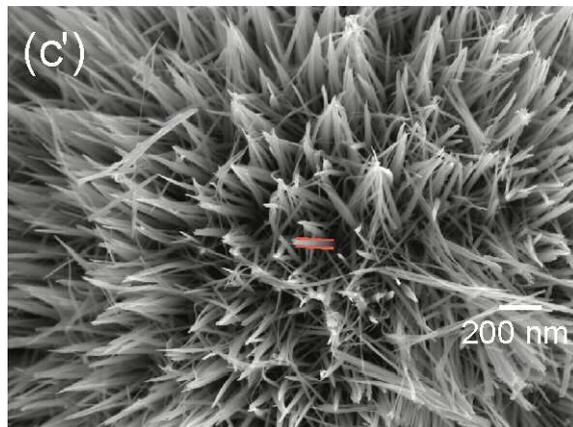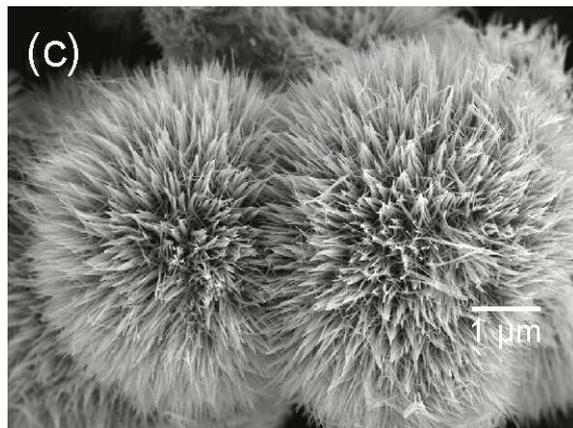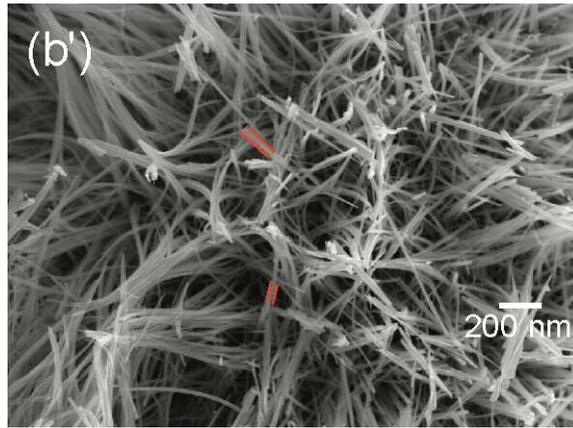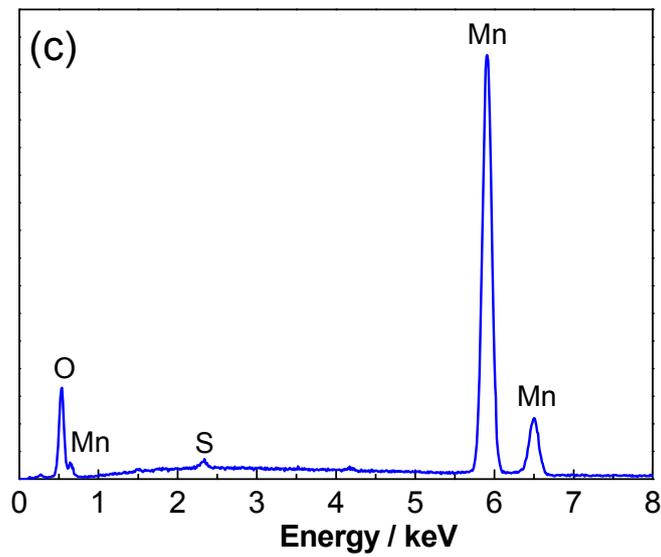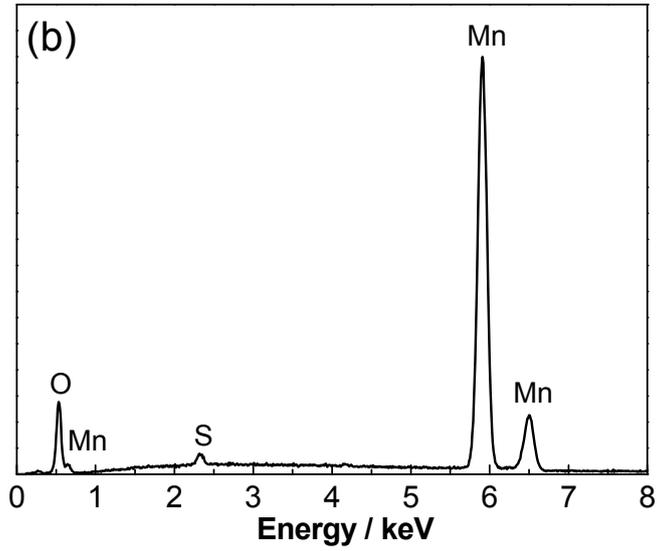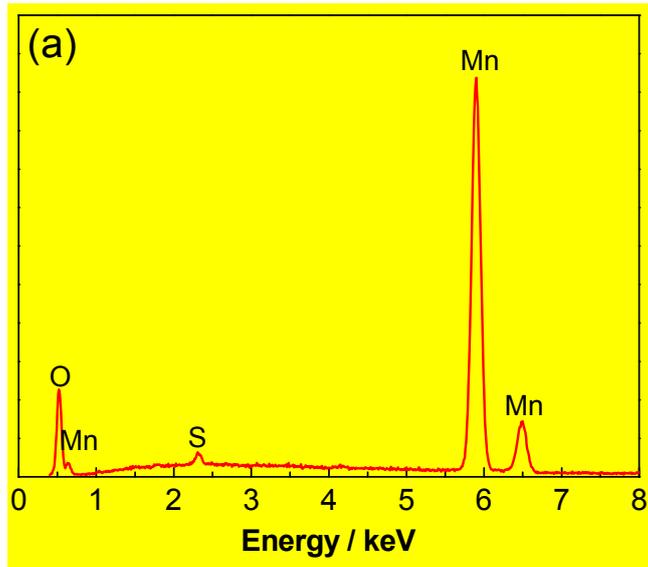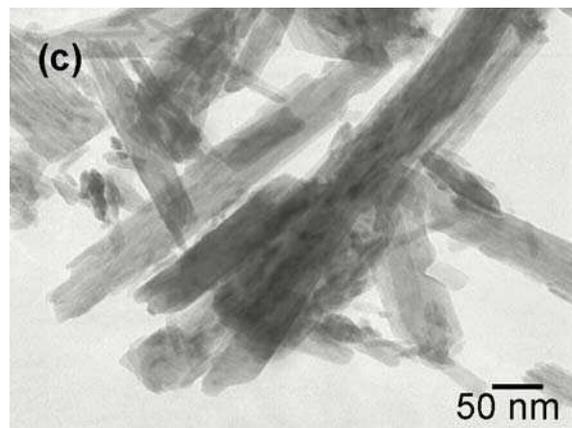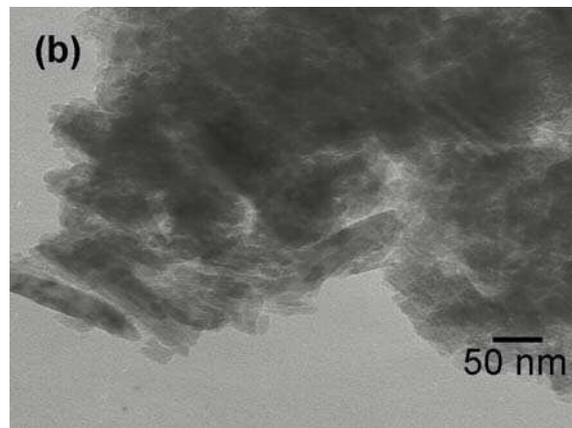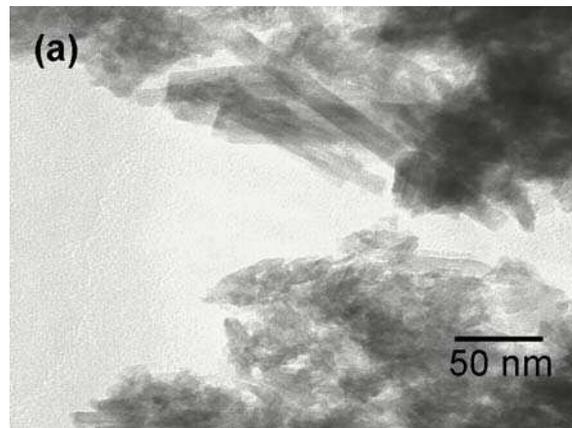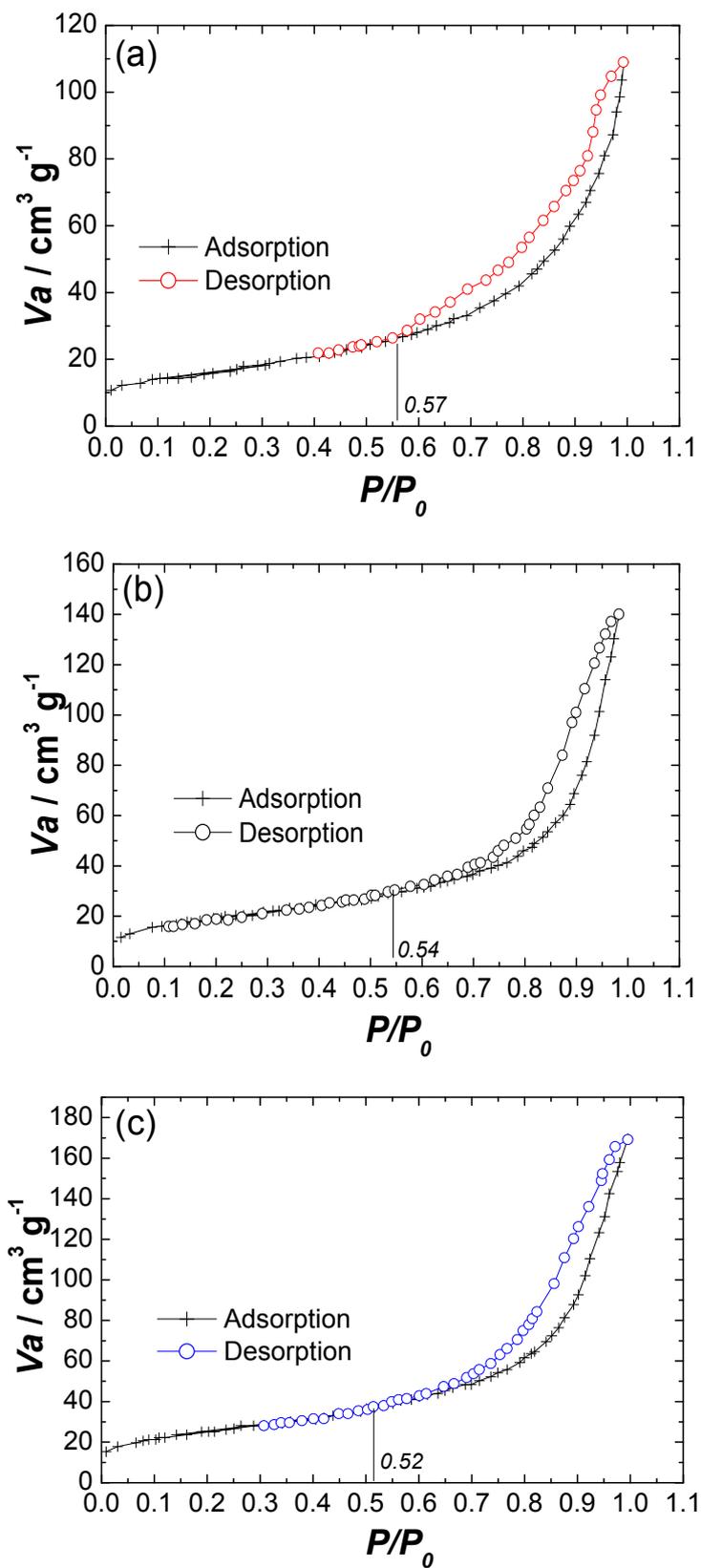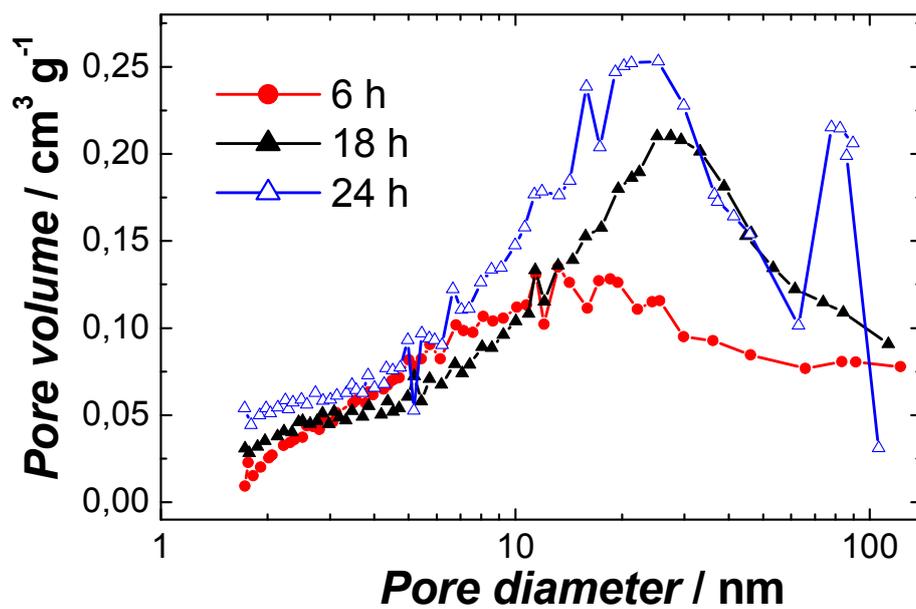
Figure 5

Figure 6
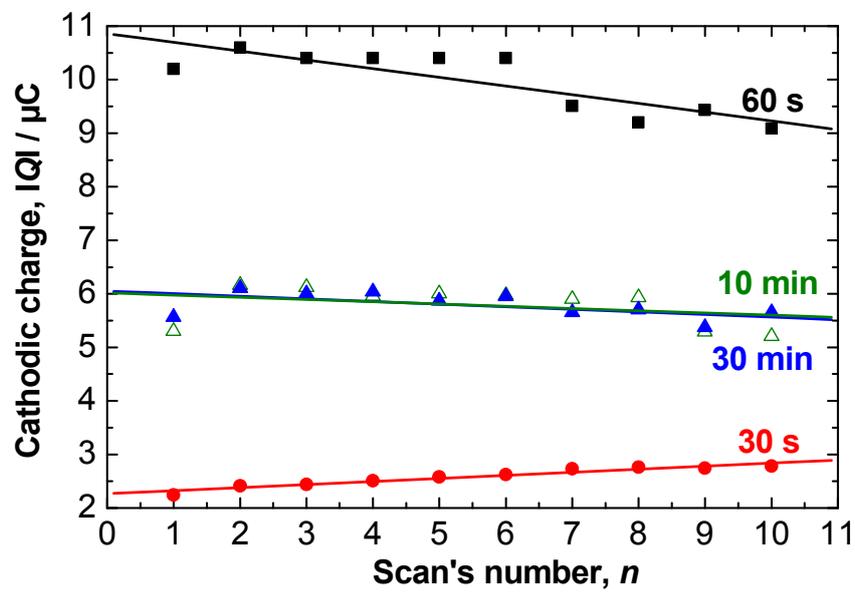
Figure 7
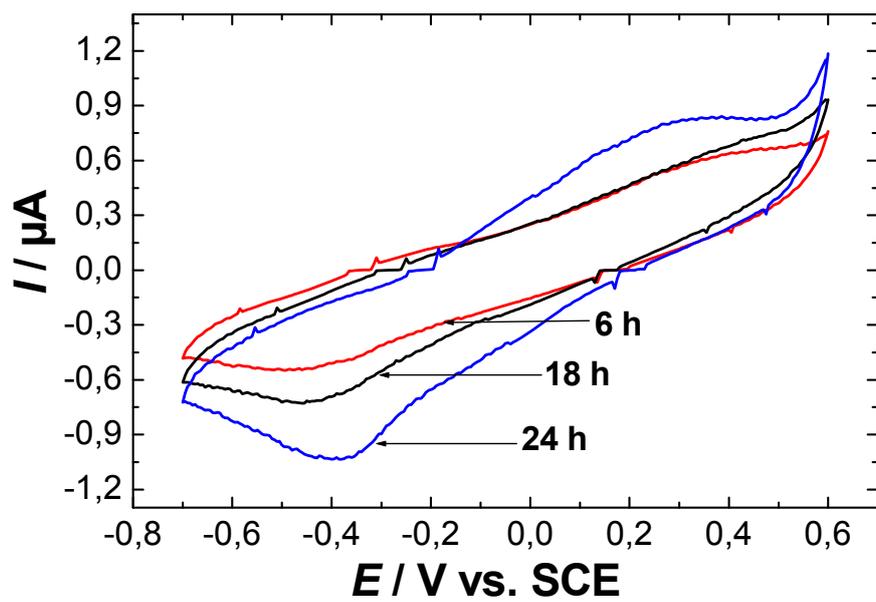
Figure 8

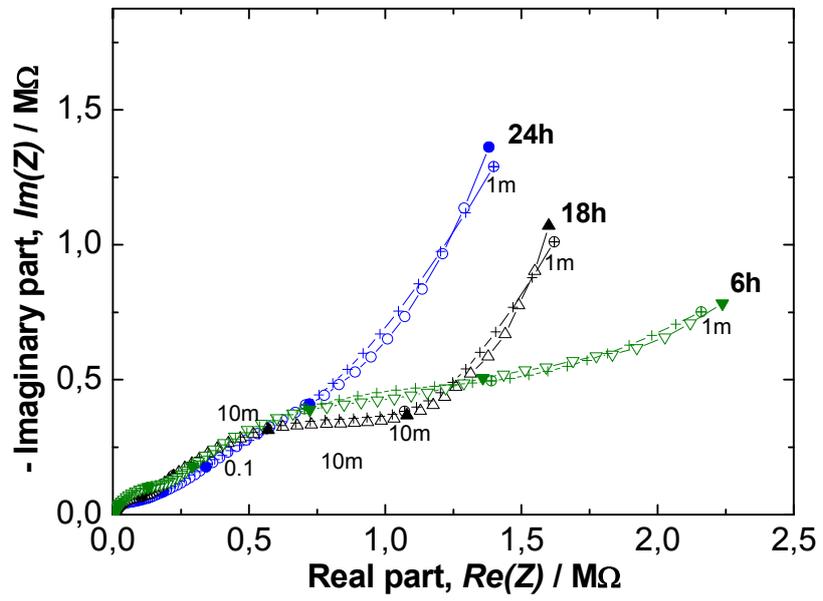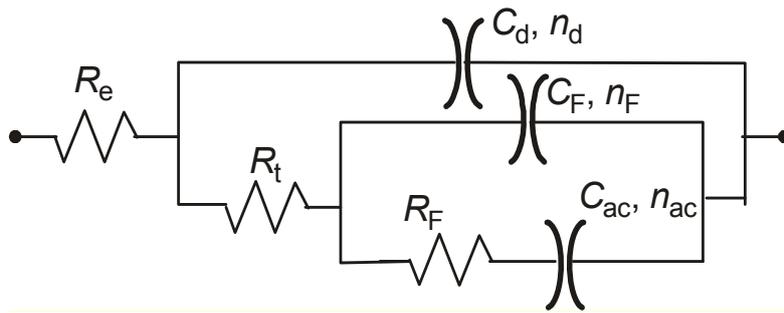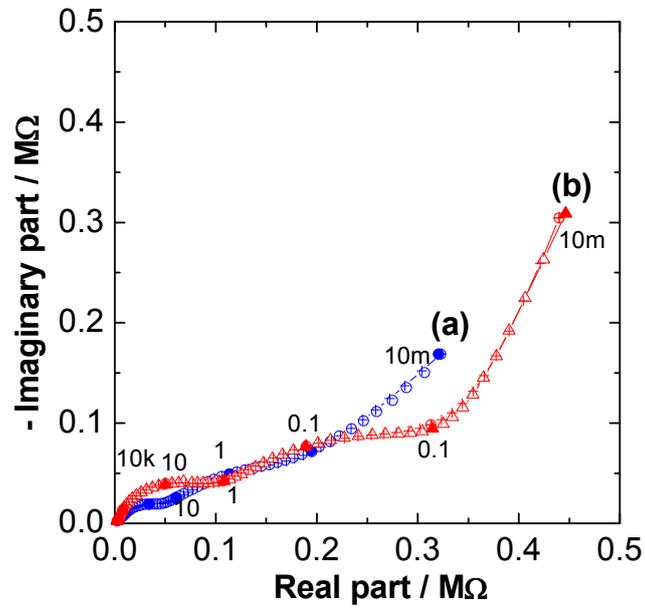Figure 9

Figure 10

Figure 11

Figure 12

Figure 13

Captions of Fig.s

Fig. 1. XRD patterns of MnO_2 powders synthesized at different durations. The (hkl) values corresponding to α-MnO_2 are given in a box.

Fig. 2. FEG-SEM images of (a), (b), (c), (d) Low and (a'), (b'), (c') high magnifications of MnO_2 powders synthesized at different durations: (a) 6 h, (b) 18 h, (c) 24 h and (d) 8 days.

Fig. 3. EDX profiles of MnO_2 powders synthesized at different durations: (a) 6 h, (b) 18 h, and (c) 24 h.

Fig. 4. TEM images of MnO_2 powders synthesized at different durations (General view): (a) 6 h, (b) 18 h and (c) 24 h.

Fig. 5. Isotherms of N_2 adsorption/desorption of the MnO_2 powders synthesized at different durations: (a) 6 h, (b) 18 h and (c) 24 h.

Fig. 6. Comparison of the distribution of the pores size of MnO_2 powders synthesized at different durations (calculated by BJH method).

Fig. 7. Polarization curves in 1 mol L^{-1} KOH of MnO_2 powders synthesized at different durations, potential scan rate 0.2 V s^{-1}.

Fig. 8. Cathodic charge as function of scan number in 1 mol L^{-1} KOH of the MnO_2 powders synthesized at different durations.

Fig. 9. Cathodic charge as function of scan rate in 1 mol L^{-1} KOH of the MnO_2 powder synthesized at 24 h.

Fig. 10. Cathodic charge as function of immersion time in 1 mol L^{-1} KOH of the MnO_2 powder synthesized at 24 h.

Fig. 11. Nyquist plots obtained in 1 mol L^{-1} KOH of MnO_2 powders synthesized at different durations and aged for 10 scans at 0.2 V s^{-1}. Symbols: Experimental and "+" regressed data with the circuit illustrated in Fig. 12.

Fig. 12. Equivalent electrical circuit to represent the EIS diagrams.

Fig. 13. Nyquist plots in 1 mol L^{-1} KOH of MnO_2 powder synthesized at 24h: (a) as-synthesized, (b) aged by 10 potential scans at 0.01 $V.s^{-1}$. Symbols: circles and triangles, experimental; +, regressed data with the circuit illustrated in Figure 12.

Caption of Table

Table 1. Pore properties of the MnO_2 powders synthesized by hydrothermal method at different durations.